Inelastic Deformation and Local Slenderness Requirements for Rectangular HSS Braces

Dawn Lehman, Charles Roeder, William Bergendahl, Joseph Kaldestad, Andrew Sen, and
Jeffrey W. Berman

ABSTRACT

Rectangular hollow structural sections (HSS) are commonly used as bracing in concentrically braced frames (CBFs) designed and detailed for seismic design requirements. As the primary yielding component in CBFs, braces are expected to sustain large inelastic axial deformation during earthquake loading. It is well known that their deformation capacity depends on the width-to-thickness ratio (local slenderness). Until 2013, HSS sections were produced to meet ASTM standard A500/A500M; after 2013, the ASTM 1085 specification was implemented, and since that time, HSS sections have also been produced to meet ASTM A1085/A1085M standards. Where the ASTM A500/A500M specification requires minimum yield and tensile stress values as well as a minimum elongation and tolerances on the wall thickness, the ASTM A1085/A1085M specification also requires a minimum Charpy V-notch (CVN) toughness, a maximum yield stress of the steel, and tighter tolerances on the wall thickness and radius of curvature of the corner. These requirements offer a more reliable brace for CBFs in seismic regions. Yet there has been limited research investigating the cyclic axial response of these members. A research study was undertaken to investigate the response of ASTM A1085/A1085M tubes using the response of ASTM A500C tubes as their reference. Forty-one brace specimens were tested under cyclic inelastic axial deformation. Comparison of the data shows that most of the ASTM A500/A500 M Grade C and ASTM A1085/1085M braces meet the respective requirements of their respective ASTM standard and that the differences between the performance of ASTM A500/A500M and ASTM A1085/1085M braces are not dramatic. In addition, the study investigated the impact of width-to-thickness ratio, global slenderness, and displacement history on the response of the braces. The data show that the current AISC 341-22 high-ductility slenderness limit for special concentrically braced frame (SCBF) braces is slightly conservative. However, the data suggest that the moderate ductility slenderness limit used for ordinary concentrically braced frame (OCBF) braces is significantly more conservative than required for consistent seismic safety. Further research is required to determine appropriate limits; this paper provides some initial recommendations based on this dataset.

Keywords: highly ductile, moderately ductile, concentrically braced frame, HSS brace, inelastic deformation.

INTRODUCTION

Rectangular hollow structural sections (HSS) are commonly used for braces in braced frames for seismic design. They have a relatively large radius of gyration, and their shape facilitates connection to gusset plates. Their inelastic performance depends on local slenderness, and AISC *Seismic Provisions for Structural Steel Buildings* (AISC, 2022), hereafter referred to as AISC 341, Table D1.1 provides local slenderness limits for highly ductile and moderately ductile braces.

For highly ductile members:

$$\frac{b}{t} < 0.65\sqrt{\frac{E}{R_yF_y}} \tag{1}$$

For moderately ductile members:

$$\frac{b}{t} < 0.76\sqrt{\frac{E}{R_yF_y}} \tag{2}$$

Design of special concentrically braced frames (SCBFs) requires sections that meet the highly ductile requirements, whereas design of ordinary concentrically braced frames (OCBFs) requires moderately ductile braces.

Rectangular HSS tubes have been manufactured under the ASTM A500/A500M (ASTM, 2021) standard. ASTM A500/A500M HSS sections are manufactured as Grades A, B, and C, which have minimum specified tensile yield stresses of 39, 46, and 50 ksi, respectively. However, most tubes are produced to meet the ASTM A500/A500M Grade C specification, and herein, reference to the ASTM A500/A500M standard is specifically to ASTM A500/A500M Grade C.

Dawn Lehman, Professor of Civil & Environmental Engineering, University of Washington, Seattle, Wash. Email: delehman@uw.edu (corresponding)

Joseph Khaldestad, Structural Engineer, Coughlin Porter Lundeen, Seattle, Wash. Email: jkaldestad@gmail.com

Will Bergendahl, Associate Project Consultant at Simpson Gumpertz & Heger, Wakefield, Mass. Email: wiberg@uw.edu

Andrew Sen, Assistant Professor of Civil Engineering, Marquette University, Milwaukee, Wis. Email: andrew.sen@marquette.edu

Jeffery Berman, Professor of Civil & Environmental Engineering, University of Washington, Seattle, Wash. Email: jwberman@uw.edu

Charles Roeder, Emeritus Professor of Civil & Environmental Engineering, University of Washington, Seattle, Wash. Email: croeder@uw.edu

In 2013, a new standard for tubes was introduced, the ASTM A1085/A1085M (ASTM, 2022) specification. In comparison to the ASTM A500 specification, the ASTM A1085 specification requires a minimum Charpy V-notch (CVN) toughness, a limit on the maximum yield stress, and tighter tolerances of the thickness of tube wall, corner radii, and mass per unit brace length. For simplicity, ASTM A500/A500M Grade C sections will be referred to as A500C and ASTM A1085/A1085M sections will be referred to as A1085.

A1085 HSS are manufactured as a single grade comparable to A500C with a specified minimum tensile yield stress of 50 ksi. Both A500C and A1085 HSS sections are formed by a cold-forming process. As a result, the HSS sections experience significant strain hardening during manufacturing, and the measured yield stresses vary and are typically significantly larger than the specified minimum yield stress. Similar variation in the measured tensile yield stress is also noted.

This variation in stress is quite critical in capacity-based provisions for seismic design. It is accounted for in the ratio of expected yield stress to the specified minimum yield stress, R_y. AISC 341 defines R_y as 1.25, 1.4, and 1.3 for A1085, A500 Grade B, and A500 Grade C, respectively. The ratios of the expected tensile stress to the specified strength for these steel grades, R_t, are 1.15, 1.3, and 1.2, respectively. Note that the lower values of R_y and R_t for the A1085 tubes typically will result in smaller design demands on the connections, which has the potential to result in a more cost-effective lateral force-resisting system (LFRS). It is noted that A_g for A500C braces is based on reduced wall thickness, whereas for A1085 sections, it is based on the full thickness; this difference might result in similar tensile force capacities for both braces.

Relative to A500 braces, far fewer research studies have focused on the cyclic response of A1085 tubes used as braces. This research study was undertaken to investigate the cyclic response of A1085 braces using A500C braces as the reference member. The test matrix for the study was developed in collaboration with structural engineers, academics, and institutes [the Steel Tube Institute (STI) and the American Institute of Steel Construction (AISC)]. A total of 41 braces were tested to investigate the following parameters: (1) HSS producer, (2) width-to-thickness ratio, b/t, (3) global slenderness ratio, KL/r, and (4) deformation history. The measured behavior of braces was then compared and used to evaluate current design provisions with an eye toward advancing the governing provisions for both OCBF and SCBF with A1085 tubes used as braces.

BACKGROUND AND LITERATURE REVIEW

A substantial body of test data is available for the inelastic behavior A500 rectangular HSS braces under cyclic loading. Sen (2018) developed a database including 70 cyclic load tests completed between 1988 and 2018. These data were used to develop improved models for the envelope, full cyclic response, and a simple yet effective deformation-based limit to predict brace fracture. The data include tests documented in 23 different papers and reports (Johnson, 2005; Herman, 2007; Kotulka, 2007; Powell, 2010; Clark, 2009; Lumpkin, 2009; Fell et al., 2009; Yang and Mahin, 2005; Uriz and Mahin, 2008; Shaback and Brown, 2003; Han et al., 2007; Lee, 1988; Liu and Goel, 1987; Sloat, 2014; Johnson, 2014; Ballard, 2015; Sen, 2014; Swatosh, 2016; Ibarra, 2018; Richard, 2009). See Sen (2018) for additional details about these prior test series.

The local slenderness limit, b/t, varied between 10.5 and 31.4 in these tests. This is a very wide slenderness range covering rectangular HSS that are both within the limits of highly ductile and moderately ductile braces as well as sections that are well above these local slenderness limits.

SCBF design is based on the hypothesis that, on average, the brace will not fracture before story drifts of approximately 2.5% in both directions (a story-drift range of 5%). The highly ductile slenderness limit is based on the need to use this inelastic deformation capacity during the maximum considered seismic event. This brace deformation capacity and the well-known moderate lateral resistance and stiffness of braced frames after brace fracture ensure that SCBFs satisfy the collapse probability limits for the maximum considered earthquake in the United States (which has an approximate return period of 2500 years depending on the location).

The cyclic axial deformation of the brace is quite different from the cyclic story drift of a braced frame. Figure 1 is a geometric illustration of this effect. The figure shows that the brace tensile elongation or compressive shortening, δ, neglecting deformation of the connections is:

$$\delta = L_f - L_i \qquad (3)$$

where L_i and L_f are the original undeformed brace length and the final deformed brace length, respectively. The horizontal story deflection, Δ, is small compared to the dimensions of the frame and the brace angle does not change significantly with increased story deflection, and so δ and Δ are related by:

$$\delta = \Delta \cos\theta \qquad (4)$$

where θ is the brace angle measured from the horizontal axis.

Normally, story drift is quantified as a ratio or percentage of the story height, H_s, which can be expressed as $H = L_i \sin\theta$. The story-drift ratio, $\dfrac{\Delta}{H_s}$, and brace elongation are related using Equation 5.

$$\frac{\delta}{L_i} = \frac{\Delta\cos\theta}{L_i} = \frac{\Delta\cos\theta}{H_s/\sin\theta} = \frac{\Delta}{H_s}\cos\theta\sin\theta \qquad (5)$$

The brace angle is typically about 45°, and $\dfrac{\delta}{L_s}$ will be $\dfrac{\Delta}{2H_s}$ for that geometry. The brace angle may vary between 30° and 60°, and $\dfrac{\delta}{L_i}$ will be $\dfrac{\sqrt{3}\Delta}{4H_s}$ at these extremes. In all cases, the axial shortening, or elongation, ratio is less than half the story-drift ratio. This geometric relationship does not depend on the system configuration.

Prior testing by Lehman et al. (2008) found that axial elongation occurs when the brace is in tension for most braced frame configurations; the exception is that most chevron-configured SCBFs do not fully yield the brace in tension even when designed with large beams intended to remain elastic under reversed cyclic loading. In contrast, most of the axial shortening resulting from compressive demands on the brace is accommodated by the geometric shortening resulting from brace bucking, as illustrated in Figure 2. The images in the figure show the progression of buckling and fracture. Initial buckling is shown in Figure 2(a); the out-of-plane deformation resulting from compression displacement demands on the brace increases with increasing story-drift demands [Figure 2(b)]. At large story-drift demands, local cupping initiates at the midpoint of the brace, as shown in Figure 2(c), due to the large compressive deformation demands on brace. Cupping occurs regardless of the b/t ratio; however, the brace deformation corresponding to cupping depends on the b/t ratio—that is, the compressive deformation initiating cupping is larger for smaller b/t ratios. As story drift increases, the global buckling deformations become very large as shown in Figure 2(b), and the cupping deformation also becomes large as shown in Figures 2(c) and 2(d). As the brace is cycled, it buckles, straightens, and buckles again, resulting in large inelastic strains that accumulate in the cupped region. Eventually local striations occur at the corners of the brace as shown in Figure 2(d). With increased cycles and deformation demands, ductile tearing initiates at the corner striations [see Figure 2(e)], and tearing progresses across the wall of the tube. Full fracture of the cross section [see Figure 2(f)] occurs after increased deformation and after the tearing has developed to a sufficient length.

After cupping, yielding in both tension and compression primarily occurs in the central cupped region; this is expected because the stresses are much larger in the cupped region due to the combination of axial load and large P-δ moments. This concentration of strain is demonstrated by measurements in this region. It is important to note that cupping deformations result from demands in the plastic hinge region, which occurs in the center of the brace under compressive loading. Note that although this appears to be wall buckling, it does not cause stability issues of the brace or the CBF system.

Sections with small local slenderness ratios, b/t, spread the cupping deformation over a significant length, and the development of local striation, tearing, and fracture are delayed until large axial deformations of the brace occur. Sections with large b/t ratios have very concentrated cupping and striations; tearing and fracture develop more quickly.

As such, the b/t ratio is one of the most important design parameters, as recognized by AISC. However, these limits were established prior to the prevalent use of A500C or the introduction of A1085 HSS sections. As such, a
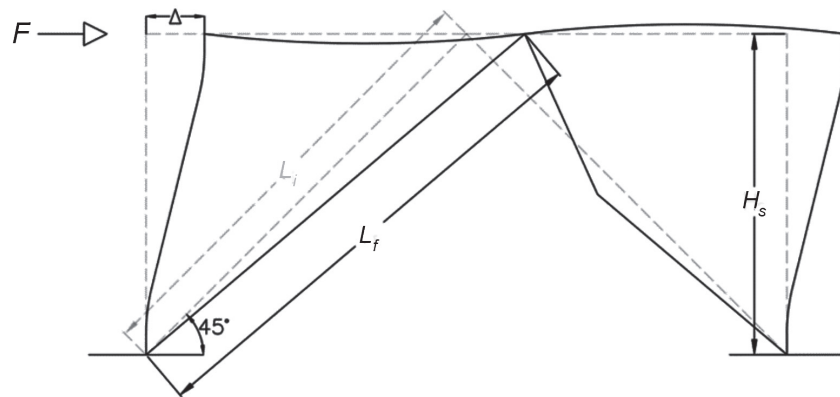

Fig. 1. Relationship between story drift and brace deformation, neglecting beam displacement.

(a) Initial brace buckling

(b) Large out-of-plane deformation

(c) Local cupping

(d) Local striations at corners

(e) Ductile tearing initiates at corners and progresses across the tube wall

(f) Fracture after ductile tearing of most of cross section

Fig. 2. Buckling, tearing, and fracture of rectangular HSS braces.

comprehensive testing program was undertaken to evaluate current design limits for both steel grades. The following presents the experimental program and results. The final section evaluates the current limits and proposes modifications to meet the intended drift limits and extend, if possible, the number of sections available to meet the highly ductile and moderately ductile limits. In addition, the testing program evaluated the influence of the HSS producer, the global slenderness ratio (KL/r) and the displacement history.

EXPERIMENTAL PROGRAM

Forty-one square HSS specimens of various sizes and steel grades were provided by four different HSS producers (Table 1). The HSS sections were tested as braces in four series at the University of Washington's Structural Research Laboratory. The tube producers are identified as "Yellow," "Red," "Blue," and "White" to maintain producer anonymity. A naming convention is used to uniquely identify each specimen, in the order listed: (1) HSS shape, (2) steel specification (A1085 or A500C), and (3) producer (Y for Yellow, R for Red, B for Blue, and W for White).

Test Series

Table 1 shows four test series that were conducted to study the range of parameters that include ASTM specification, producer, length (and therefore KL/r), loading protocol, and HSS section (and therefore b/t). Test series I and II included a total of 32 tests that focused on the impact of producer, ASTM specification, and HSS section; all tests in these series had a brace length of 237.5 in. (6033 mm) and were tested under a standard increasing amplitude cyclic loading protocol as described later. Series I consisted of A500 and A1085 braces in the full range of section sizes, where the Yellow producer provided all A1085 braces and a mix of the four producers provided the A500 braces.

Test series III investigated solely A1085 HSS with a length of 237.5 in. (6033 mm) to study the impact of displacement histories; prior research suggests that the performance of HSS braces depends on the deformation history (Fell et al., 2009). Specifically, HSS8×8×⅜, HSS7×7×⅜, and HSS5×5×⅜ braces all from the producer marked Yellow were tested using three different loading protocols. These sections were selected because they provide a substantial range of local slenderness. As Table 1 shows, the loading protocol used for most tests was a symmetric protocol based on ATC-24 recommendations (ATC, 1992). Two alternative loading protocols identified as "chevron" or "near fault" were used in Test series III. The chevron protocol was compression dominant and intended to represent the behavior of a brace within an SCBF with a chevron configuration (Roeder et al., 2019). The near-fault loading protocol was tension dominant and intended to represent the pulse demands of a near-fault ground motion (Fell et al., 2009). Additional details on the loading protocols are provided in a subsequent section.

Prior research has shown that deformation capacity of HSS braces is also a function of the global-slenderness ratio, KL/r. To investigate this, Series IV tested A1085 HSS8×8×⅜, HSS7×7×⅜, and HSS5×5×⅜ braces that were all from the Yellow producer and were 184 in. (4660 mm) long such that their response could be compared with that of the braces that were 238 in. (6033 mm) long. Series IV specimens were subjected to the symmetric cyclic loading protocol with increasing displacements, but the magnitude of displacements was scaled to be proportional to the brace length and have the same normalized deformation history. These shorter specimens had "Short" appended to their designations.

Test Setup

The test setup was designed and built to impose cyclic compressive and tensile axial deformations on the brace specimens (HSS or other sections used as braces including BRBs). A drawing of the setup is shown in Figure 3(a); a photograph of the setup with a brace specimen in place is shown in Figure 3(b). The premise of the setup is to subject an HSS section attached to tapered plates at each end to the specified cyclic axial displacement history.

Two actuators with a combined capacity of 1,000 kips (4448kN) and +10 in. (25.4 cm) of stroke were used to impose the specified displacement demand under displacement control. The actuators were attached to a sliding beam on one side and a fixed reaction block on the other [Figure 3(a)].

The sliding load beam shown was an ASTM A992/A992M (ASTM, 2020) W33×201 section with ¾ in. side plates welded to the flanges on both sides to form a box section. The box section was filled with concrete to increase its stiffness. Low-friction polytetrafluoroethylene (PTFE) on greased and polished stainless-steel surfaces facilitated the sliding action with minimal lost resistance. Doubled shear plate connections were attached to the sliding beam and the central anchor block, and the gusset plate connections at each end of the brace fit between the shear plates and was shimmed as needed [Figure 3(c)]. The bolted connection was conservatively designed with 1 in. (25 mm) ASTM F3125/F3125M Gr. A490 (ASTM, 2019) bolts in double shear to minimize local slip and avoid local yielding. The gusset plates were designed by the balanced design procedure to develop the expected capacities of the specific brace section (Roeder et al., 2011).

Extensive instrumentation was attached to each specimen to measure the applied loads and deformations, as well as the distribution of strains and deformations, including out-of-plane (buckling) response. Axial load was measured

Table 1. HSS Sections, Brace Lengths, ASTM Specifications, Producers, and Loading Protocols Used in the Four Test Series Conducted

ASTM Specification	A500C							A1085			
Producer	Yellow	Red	Blue	White	Yellow			Yellow	Red	Blue	White
Length (mm) (1 mm = 0.039 in.)	6033	6033	6033	6033	6033			4660	6033	6033	6033
Load Protocol	Symmetric Cyclic	Symmetric Cyclic	Symmetric Cyclic	Symmetric Cyclic	Symmetric Cyclic	Chevron	Near Fault	Symmetric Cyclic	Symmetric Cyclic	Symmetric Cyclic	Symmetric Cyclic
HSS Section											
10×10×3/8				Series I	Series I						
8×8×1/2				Series I	Series I				Series II	Series II	Series II
8×8×3/8				Series I	Series I/III	Series III	Series III	Series IV	Series II	Series II	Series II
7×7×1/2			Series I		Series I			Series IV			
7×7×3/8	Series I				Series I/III	Series III	Series III				
7×7×5/16	Series I				Series I						
6×6×1/2		Series I			Series I						
6×6×3/8		Series I			Series I				Series II	Series II	Series II
6×6×5/16		Series I			Series I						
5×5×3/8	Series I				Series I/III	Series III	Series III	Series IV	Series II	Series II	Series II

with load cells attached to the actuators. A series of string potentiometers measured axial and out-of-plane deformations of the brace. Strain gauges were attached at the quarter points of the brace to measure axial force and bending moments since the brace remains nearly elastic outside the central region and the regions attached to and near the gusset plates. A noncontact instrumentation system, the Optotrak system by Northern Digital Inc., was used to measure three-dimensional displacements at different locations along the brace. The Optotrak works by observing the movement of affixed LEDs with a special set of cameras and to within a millimeter. LEDs were concentrated within the gusset plate and the end of the brace—that is, the regions where significant inelastic action was expected. The measurements are used to determine local inelastic deformations and strain

estimates and to provide a redundant check of key potentiometer readings. Duncan linear potentiometers are also placed at various location where small movements are possible to ensure functionality of the test and test setup. For this setup and instrumentation, the direction of buckling must be controlled in the experiment. To achieve this, each brace was welded to the gusset plate with a small, predetermined eccentricity.

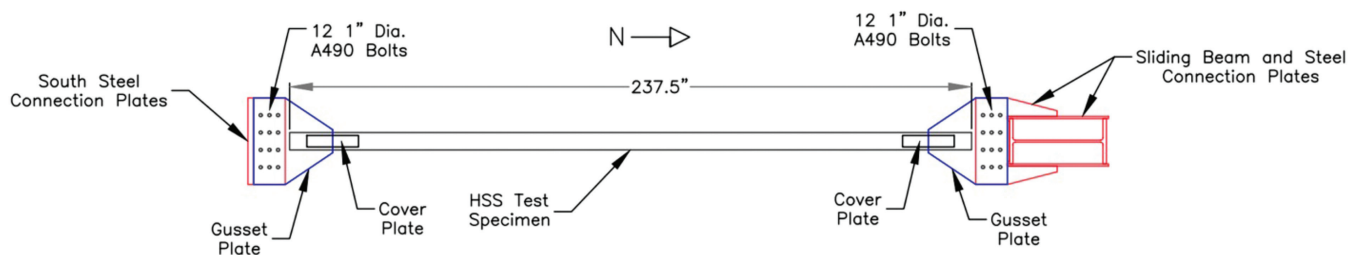**MATERIAL PROPERTIES OF TEST SPECIMENS**

Yield stress and tensile stress, the CVN toughness, and the steel thickness were measured for each supplied HSS steel section (including those of the name nominal dimension from different suppliers). All CVN tests were conducted
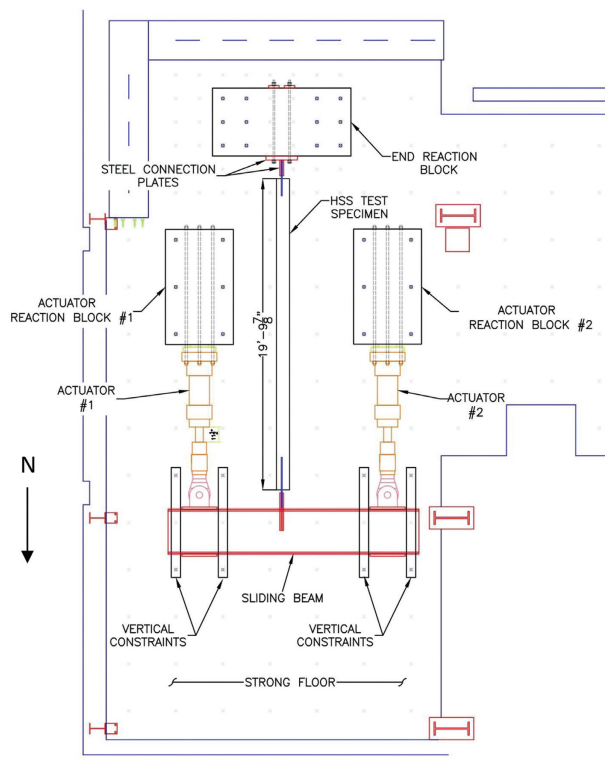
(a) Test setup

(b) Setup with a specimen in place

(c) Typical brace and bolted connection

Fig. 3. Test setup and brace specimen connection.

at room temperature. These properties were evaluated and compared to the ASTM standards. In addition, comparisons were made between A500 and A1085 tubes and between different producers of tubes. Table 2 summarizes the measured yield, tensile stress, and CVN toughness for each section produced by each producer. Tube wall thicknesses were measured; all of the thicknesses were within the tolerance of the respected ASTM standard.

As expected, the yield and tensile stress within each ASTM specification varied because of the cold-forming process, but the variation is within the tolerances of the respective ASTM standards. The following statistics were calculated using all of the HSS braces tested as part of this research program.

- The average measured yield stress was 63.95 ksi with a standard deviation of 4.49 ksi.

- The average R_y value was 1.28 with a standard deviation 0.09.

- The average tensile stress was 72.58 ksi with a standard deviation of 4.13 ksi.

- The average R_t value was 1.13 with a standard deviation of 0.066.

Most importantly, the difference between the A500C and A1085 tests was relatively small compared to the standard deviation of the overall data. This suggests that A500C HSS sections outperform expectations because they meet some or all of the requirements of the A1085 standard.

Three CVN tests were completed for each specimen and the reported toughness in Table 2 is the mean value of the three tests. The average CVN toughness for all specimens is 82 ft-lb. This number is somewhat low because energy larger than 120 ft-lb could not be measured, and specimens designated as 120+ exceeded this value.

The average CVN toughness for the A500C specimens was 62 ft-lb, which is approximately 75% of the average value of the A1085 specimens. It is noted that many of the specimens were subsize because the thickness of the steel was less than the size required for the standard CVN test. The subsize specimens are identified with the asterisk in the table, and their CVN toughness values were adjusted by the relative thickness of the specimen. This adjustment appears reasonable and is recommended in ASTM A370 (ASTM, 2023), but there is little documentation to verify that it is appropriate or correct. As a result, the toughness data must be viewed with caution. With this adjustment, two sections fell slightly below the 20 ft-lb limit for A1085 tubes.

Nearly all the toughness specimens were taken from the flat portion of the tube. However, specimens were taken from the corners of two of the thicker tubes. The values from the corners might be smaller than the actual value because of cold working. The CVN toughness of the six

coupons taken for the corners were significantly tougher (nearly twice the value) than the CVN toughness taken from the flats of the same tube.

The thickness of all tubes was measured with a micrometer. The variation was well within the tolerances of the A500C and A1085 standards. In general, these combined data suggest that A1085 may consistently have slightly greater CVN toughness, but the overall the difference between the A1085 and A500C tubes is not significant.

TEST PROTOCOLS

The tests in this program were conducted by applying quasi-static cyclic axial displacements to one end of the brace while the other end of the brace was pinned. The two actuators were programmed to run under identical displacement control using MTS Multipurpose Testware software (MTS, 2011). In all cases, tests started with very small cycles at a displacement amplitude of 1¹⁄₁₆ in. to ensure that all equipment was functioning correctly. Then small but increasing amplitude cycles were applied until initial brace buckling and tensile yielding occurred.

One of three different displacement histories were applied to each test specimen. Figure 4(a) shows a displacement history based on the ATC-24 protocol (ATC, 1992). The history is symmetric, with displacement amplitudes based on a multiplier times the initial yield deformation until failure. The yield and buckling displacements were determined as a function of the brace length, as served as the basis for the displacement history applied to each brace. Figure 4(a) shows the deflections that were applied to the long (238 in.) specimens. The protocol for the short specimens is the same shape but scaled to the smaller deformations calculated for yield and buckling.

The chevron displacement protocol, shown in Figure 4(b), was based on previous research that showed that beam deflection in chevron configurations results in increased compressive deformations and decreased tensile deformations (Roeder et al., 2019). In this displacement protocol, the target compressive displacements increased in the same progression as the symmetric protocol. However, after initial yielding the tension cycles are limited to the deformation at which the brace axial tension force reaches the magnitude of the recorded brace buckling load.

The near-fault displacement protocol, shown in Figure 4(c), was developed as a modified version of a loading protocol used in previous research to represent nonsymmetric pulse-type demands for a braced frame subjected to near-fault ground motions (Fell et al., 2009). This protocol follows the shape of the compression-dominated near-field loading protocol used by Fell, but this protocol was inverted to be tension dominated and the magnitude of displacements was modified to reflect the buckling and yield deformations.

Table 2. Measured Properties for Test Specimens					
HSS Section	Yield Stress (ksi)	Yield Stress Ratio	Tensile Stress (ksi)	Tensile Stress Ratio	Percent Elongation (%)	CVN Energy (ft-lb)
5×5×⅜ A500 Y	65.38	1.31	71.9	1.16	30.79	17.0*
5×5×⅜ A1085 Y	66.04	1.32	74.6	1.15	32.83	25.0*
6×6×5⁄16 A500 R	57.37	1.15	72.8	1.17	34.65	81.6*
6×6×5⁄16 A1085 Y	62.07	1.24	71.9	1.11	34.11	46.0*
6×6×⅜ A500 R	61.19	1.22	76.4	1.23	35.36	56.5*
6×6×⅜ A1085 Y	66.81	1.34	72.6	1.12	31.86	25.0*
6×6×½ A500 R	62.84	1.26	67.1	1.08	33.48	120+
6×6×½ A1085 Y	67.85	1.36	72.0	1.11	34.88	27.8
7×7×5⁄16 A500 Y	62.71	1.25	70.0	1.13	31.16	23.6*
7×7×5⁄16 A1085 Y	57.70	1.15	64.1	0.99	33.12	27.8*
7×7×⅜ A500 Y	61.35	1.23	72.2	1.16	30.76	19.0*
7×7×⅜ A1085 Y	61.89	1.24	70.1	1.08	31.32	23.0*
7×7×½ A500 B	57.82	1.16	69.1	1.11	29.6	42.0
7×7×½ A1085 Y	64.38	1.29	71.7	1.10	32.7	28.7
8×8×⅜ A500 W	66.19	1.32	76.5	1.23	34.44	87.1*
8×8×⅜ A1085 Y	60.37	1.21	72.1	1.11	34.2	11.3*
8×8×½ A500 W	65.47	1.31	72.0	1.16	34.27	67.3
8×8×½ A1085 Y	64.42	1.29	75.4	1.16	32.23	40.3
10×10×⅜ A500 W	59.02	1.18	69.5	1.12	34.2	120+*
10×10×⅜ A1085 Y	58.34	1.17	73.8	1.14	34.94	27.5*
5×5×⅜ A1085 R	68.82	1.38	77.52	1.19	34.92	30.9*
5×5×⅜ A1085 W	69.53	1.39	75.03	1.15	38.06	102.4*
5×5×⅜ A1085 B	78.15	1.56	87.62	1.35	27.90	40.9*
6×6×⅜ A1085 R	60.41	1.21	74.29	1.14	33.26	54.0*
6×6×⅜ A1085 W	67.66	1.35	73.22	1.13	37.53	110.2*
6×6×⅜ A1085 B	69.05	1.38	73.59	1.13	34.75	120+*
8×8×⅜ A1085 R	61.20	1.22	75.42	1.16	32.44	77.8*
8×8×⅜ A1085 W	63.19	1.26	70.67	1.09	40.55	94.0*
8×8×⅜ A1085 B	68.24	1.36	71.63	1.10	37.18	120+*
8×8×½ A1085 R	58.54	1.17	64.27	0.99	34.43	120+
8×8×½ A1085 W	58.54	1.17	64.27	0.99	42.02	120+
8×8×½ A1085 B	66.36	1.33	70.51	1.08	39.56	120+

* Indicates tests that were conducted with a subsize Charpy test specimen and with toughness values adjusted by the ratio of the thickness of a standard Charpy specimen to the subsize specimen.
+ Indicates specimen that reached the maximum energy that could be measured.

EXPERIMENTAL RESULTS

For each specimen, the load-displacement response was measured. In addition, the progressive yielding and damage to the specimens was observed during the tests and noted. To determine the damage states and their corresponding deformation demand, clear damage criteria were established as shown in Table 3. These damage states were developed in prior research (Roeder et al., 2012) and relate to potential repair costs and the sequence of behaviors leading to brace fracture as summarized earlier and described in prior research (Lehman et al., 2008). For the brace alone,

the important damage states (DS) on the degree of buckling (DS B1- B3) as well as brace tearing (DS B3-T) and fracture (DS B4) result from cyclic loading and cupping of the tube walls in the plastic hinge region.

Forty-one tests were completed. Table 4 summarizes the results, where P_{Tmax} is the brace maximum tension force, P_{Cmax} is the maximum brace compression force, P_y is the brace yield force calculated with measured material properties, P_{cr} is the brace buckling force calculated with measured material properties, $\Delta_{T,max}$ is the maximum brace elongation in tension prior to brace fracture, $\Delta_{C,max}$ is the maximum brace compressive deformation, Δ_{Acc} is the cumulative brace deformation, $\sum E_{Diss}$ is the cumulative energy dissipation, $A_{g,m}$ is the measured cross-sectional area, and $F_{y,m}$ is the measured yield strength. The last column in Table 4 is the accumulated energy dissipated prior to brace fracture normalized to the tensile force predicted from the measured properties of the tube. This measure is an approximate and relative comparison of the stable cyclic, nonlinear response achieved by each specimen.

Four tests of series I and II are presented in greater detail—specifically, specimen 5×5×⅜ A1085 Y, specimen 6×6×⅜ A1085 Y, specimen 7×7×⅜ A1085 Y, and specimen 8×8×⅜ A1085 Y. These specimens were selected because they have the following properties in common: (1) A1085 HSS sections, (2) same nominal thickness, and (3) same producer. This permits direct comparison based on varied design parameters—that is, the global and local slenderness ratios. Specifically, the four tests have b/t ratios of 10.3, 13, 14.2, and 18.3, which represent members well below the high ductility slenderness limit, members approaching the high ductility limit, members exceeding the high ductility limit and approaching the moderate ductility limit, and members clearly exceeding the moderate ductility limit. Results for series III and IV are focused on a single parameter and are discussed separately.

Impact of Width-to-Thickness Ratio

Figure 5 shows the axial force/deformation plots for the highlighted specimens (highlighted specimens are shaded in Table 4), and Figure 6 provides photos of these specimens at the maximum compressive deformation prior to initiation of tearing. The following summarizes the observed and measured response of each of the highlighted specimens.
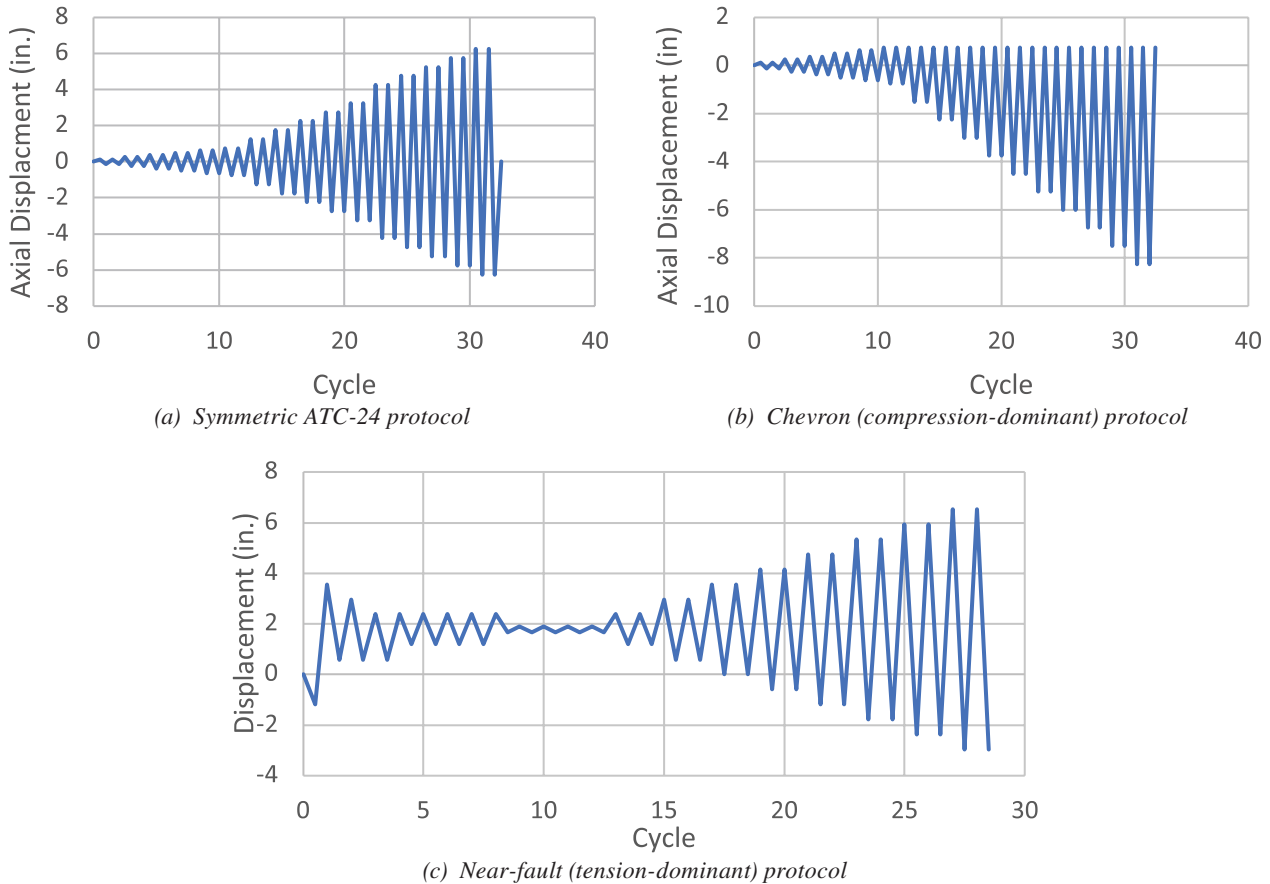

(a) Symmetric ATC-24 protocol

(b) Chevron (compression-dominant) protocol

(c) Near-fault (tension-dominant) protocol

Fig. 4. Test protocols.

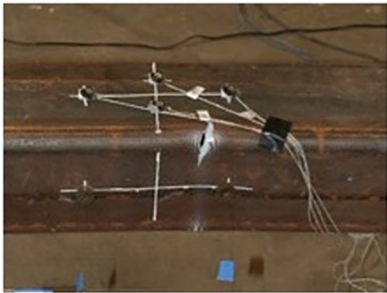| Table 3. Brace Damage States for Performance Assessment			
Sketch/Photograph of Damage State	**Abbreviation**	**Damage State**	**Description**
	B1	Initial global buckling	Brace midspan deflection visible but less than the brace depth
	B2	Moderate global buckling	Brace midspan deflection exceeds the brace depth
	B3 – C	Local cupping deformations	Visible local cupping deformation near midpoint of the brace
	B3 – T	Striations and tearing	Striation lines begin in the cupped (plastic hinge) region of brace
	B4	Brace fracture	Brace fractures through the entire cross section
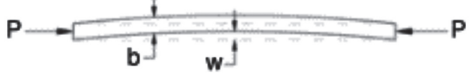
| Table 4. Summary of Test Specimen Performance with Highlighted Specimens Indicated							
HSS Section	$P_{T,max}$ (kips) $(P_{T,max}/P_y)$	$P_{C,max}$ (kips) $(P_{C,max}/P_{Cr})$	$\Delta_{T,max}$ (in.) (Drift %)	$\Delta_{C,max}$ (in.) (Drift %)	Δ_{range} (in.) (Drift %)	Δ_{Acc} (in.) (Drift %)	$\dfrac{\sum E_{Diss}}{A_{g,m}F_{y,m}}$
5×5×⅜ A500 Y	432.50 (1.04)	−95.30 (0.99)	5.13 (4.28)	4.89 (4.07)	10.02 (8.35)	119.54 (99.65)	20.57
5×5×⅜ A1085 Y	443.60 (1.02)	−98.38 (0.97)	5.25 (4.38)	5.50 (4.59)	10.75 (8.96)	132.02 (110.05)	21.74
6×6×⁵⁄₁₆ A500 R	409.70 (1.06)	−125.75 (0.82)	3.06 (2.55)	3.26 (2.71)	6.31 (5.26)	52.34 (43.63)	13.29
6×6×⁵⁄₁₆ A1085 Y	456.40 (1.07)	139.80 (0.87)	3.13 (2.61)	3.12 (2.60)	6.25 (5.21)	51.33 (42.79)	12.57
6×6×⅜ A500 R	511.00 (1.05)	−168.70 (0.96)	3.74 (3.12)	3.72 (3.10)	7.46 (6.22)	65.80 (54.85)	16.45
6×6×⅜ A1085 Y	547.90 (1.01)	−180.00 (0.97)	3.52 (2.93)	3.52 (2.93)	7.04 (5.87)	56.61 (47.19)	13.63
6×6×½ A500 R	646.20 (1.02)	−218.70 (1.01)	4.45 (3.71)	4.06 (3.39)	8.51 (7.10)	80.64 (67.22)	17.25
6×6×½ A1085 Y	727.20 (1.06)	−218.60 (0.97)	4.67 (3.89)	5.12 (4.27)	9.79 (8.16)	97.41 (81.21)	22.36
7×7×⁵⁄₁₆ A500 Y	496.60 (1.05)	−209.80 (0.88)	1.73 (1.44)	1.83 (1.53)	3.56 (2.97)	20.29 (16.91)	5.82
7×7×⁵⁄₁₆ A1085 Y	478.10 (1.05)	−201.50 (0.80)	1.99 (1.66)	2.31 (1.92)	4.29 (3.58)	27.94 (23.30)	8.01
7×7×⅜ A500 Y	570.90 (1.06)	−231.80 (0.83)	2.51 (2.09)	2.79 (2.33)	5.30 (4.42)	35.26 (29.40)	10.49
7×7×⅜ A1085 Y	615.90 (1.07)	−254.90 (0.87)	2.36 (1.97)	2.85 (2.38)	5.21 (4.35)	37.42 (31.20)	9.76
7×7×½ A500 B	710.40 (1.06)	−278.80 (0.80)	3.59 (2.99)	4.16 (3.47)	7.75 (6.46)	70.86 (59.08)	19.31
7×7×½ A1085 Y	805.10 (1.04)	−305.70 (0.84)	3.48 (2.90)	4.41 (3.68)	7.89 (6.58)	70.13 (58.46)	18.21
8×8×⅜ A500 W	702.70 (1.02)	−359.98 (0.93)	1.24 (1.04)	1.90 (1.58)	3.14 (2.62)	18.10 (15.09)	4.97
8×8×⅜ A1085 Y	672.60 (1.02)	−328.80 (0.81)	2.18 (1.82)	2.18 (1.82)	4.36 (3.63)	27.43 (22.87)	9.18
8×8×½ A500 W	905.97 (1.03)	−434.72 (0.88)	2.71 (2.26)	2.80 (2.34)	5.51 (4.60)	38.25 (31.89)	12.66
8×8×½ A1085 Y	921.90 (1.02)	−418.20 (0.82)	2.96 (2.46)	3.32 (2.77)	6.28 (5.23)	44.07 (36.74)	13.29
10×10×⅜ A500 W	785.40 (1.01)	−480.10 (0.79)	2.10 (1.75)	2.48 (2.07)	4.58 (3.81)	25.71 (21.43)	5.96
10×10×⅜ A1085 Y	812.80 (1.01)	−507.60 (0.81)	1.60 (1.33)	1.84 (1.53)	3.44 (2.87)	15.66 (13.05)	4.67
5×5×⅜ A1085 R	456.59 (1.01)	−114.23 (1.13)	4.91 (4.09)	5.14 (4.29)	10.05 (8.38)	120.09 (100.11)	18.79

	$P_{T,max}$ (kips) $(P_{T,max}/P_y)$	$P_{C,max}$ (kips) $(P_{C,max}/P_{Cr})$	$\Delta_{T,max}$ (in.) (Drift %)	$\Delta_{C,max}$ (in.) (Drift %)	Δ_{range} (in.) (Drift %)	Δ_{Acc} (in.) (Drift %)	$\dfrac{\Sigma E_{Diss}}{A_{g,m}F_{y,m}}$
HSS Section							
5×5×⅜ A1085 W	468.27 (1.03)	−110.19 (1.09)	4.72 (3.93)	5.27 (4.39)	9.99 (8.32)	109.31 (91.13)	17.64
5×5×⅜ A1085 B	538.20 (1.03)	−126.44 (1.25)	3.93 (3.28)	5.07 (4.23)	9.00 (7.51)	98.28 (81.93)	15.50
6×6×⅜ A1085 R	521.04 (1.08)	−178.82 (0.97)	3.96 (3.30)	4.14 (3.45)	8.09 (6.75)	73.05 (60.89)	17.30
6×6×⅜ A1085 W	549.55 (1.00)	−185.84 (1.00)	3.66 (3.05)	4.04 (3.37)	7.70 (6.42)	65.74 (54.81)	14.62
6×6×⅜ A1085 B	581.67 (1.03)	−177.88 (0.96)	2.97 (2.48)	3.26 (2.72)	6.23 (5.19)	50.27 (41.91)	10.74
8×8×⅜ A1085 R	660.41 (0.99)	−323.69 (0.80)	2.68 (2.23)	1.77 (1.48)	4.45 (3.71)	25.76 (21.48)	8.17
8×8×⅜ A1085 W	711.95 (1.02)	−361.03 (0.89)	2.31 (1.93)	2.28 (1.90)	4.59 (3.83)	26.46 (22.06)	8.30
8×8×⅜ A1085 B	763.00 (1.01)	−363.94 (0.90)	1.74 (1.45)	2.55 (2.12)	4.29 (3.57)	24.55 (20.47)	6.71
8×8×½ A1085 R	819.18 (1.04)	−425.29 (0.83)	3.31 (2.76)	2.95 (2.46)	6.26 (5.21)	47.25 (39.39)	11.77
8×8×½ A1085 W	964.72 (1.01)	−446.26 (0.87)	2.83 (2.36)	3.28 (2.73)	6.10 (5.09)	45.42 (37.86)	13.10
8×8×½ A1085 B	938.58 (0.98)	−478.57 (0.94)	3.03 (2.53)	3.05 (2.55)	6.08 (5.07)	39.67 (33.07)	10.93
5×5×⅜ A1085 Y Chevron	409.06 (0.94)	−93.31 (0.92)	3.64 (3.03)	7.82 (6.52)	11.46 (9.55)	229.47 (191.30)	23.12
5×5×⅜ A1085 Y Near Fault	464.24 (1.07)	−95.36 (0.94)	7.88 (6.57)	4.34 (3.62)	12.22 (10.19)	152.72 (127.32)	24.92
7×7×⅜ A1085 Y Chevron	258.35 (0.45)	−257.40 (0.88)	1.16 (0.97)	4.24 (3.54)	5.41 (4.51)	34.04 (28.37)	5.81
7×7×⅜ A1085 Y Near Fault	670.92 (1.16)	−255.17 (0.87)	4.08 (3.40)	1.50 (1.25)	5.57 (4.65)	42.55 (35.47)	12.78
8×8×⅜ A1085 Y Chevron	332.92 (0.50)	−320.72 (0.79)	1.10 (0.92)	3.58 (2.98)	4.68 (3.90)	25.74 (21.46)	5.32
8×8×⅜ A1085 Y Near Fault	716.32 (1.08)	−308.41 (0.76)	3.95 (3.29)	1.03 (0.86)	4.98 (4.15)	32.37 (26.98)	11.43
5×5×⅜ A1085 Y Short	438.58 (1.01)	−140.80 (0.83)	3.64 (3.93)	3.45 (3.73)	7.10 (7.66)	76.29 (63.60)	15.94
7×7×⅜ A1085 Y Short	617.53 (1.07)	−327.91 (0.84)	1.56 (1.68)	1.74 (1.88)	3.30 (3.57)	19.88 (16.57)	7.10
8×8×⅜ A1085 Y Short	666.42 (1.01)	−393.60 (0.78)	1.61 (1.74)	1.65 (1.78)	3.27 (3.52)	19.70 (16.42)	6.98

Table 4. Summary of Test Specimen Performance with Highlighted Specimens Indicated (continued)

Specimen 5×5×⅜ A1085 Y buckled at a compressive load of 98.4 kips, which is the peak compressive force, at a compressive axial displacement of 0.19 in. The B2 damage state was noted during the 1.25 in. compressive-displacement cycles. The specimen reached a maximum tensile force of 443.6 kips at an axial displacement of 1.83 in., and the tensile forces slowly decreased during later cycles. Local cupping at the center of the specimen was observed at a compressive axial displacement of just over 5 in. Tearing at the center of the specimen was initially observed during the second cycle of the 5.75 in. target displacement, and the tearing quickly spread across the east, top, and bottom walls of the section. The brace fractured in tension during this same cycle, at an axial displacement of 5.25 in.

Specimen 6×6×⅜ A1085 Y buckled at a compressive force of 180 kips at a displacement of 0.15 in. The B2

damage state was observed during the 1.75 in. target displacement cycles. This specimen reached a peak tensile force of 547.9 kips at an axial displacement of 1.76 in., and the peak tensile forces decreased slightly in subsequent cycles at larger displacements. Local cupping deformations were initially observed at an axial displacement of about 3.06 in. Striations and tearing developed at the center of the brace during the second cycle of this 3.75 in. target displacement, but the brace did not fracture at the peak tensile displacement. Only the west wall of the specimen remained intact, and when the loading was reversed and the brace was put into compression, it fractured at a displacement of 0.55 in. prior to reaching its neutral position.
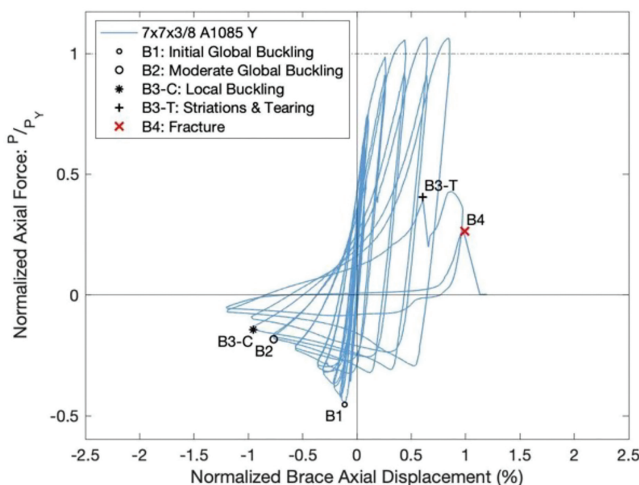
Specimen 7×7×⅜ A1085 Y buckled at a compressive force of 254.9 kips at a displacement of 0.27 in. Local cupping was observed at a compressive displacement of 2.27 in.
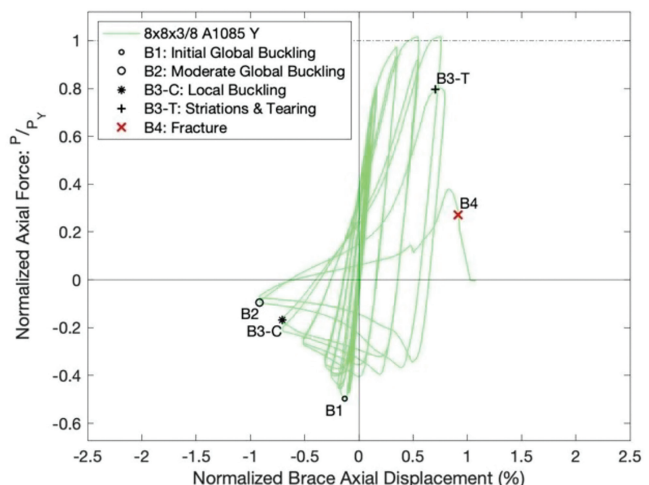

(a) 5×5×⅜ A1085 Y

(b) 6×6×⅜ A1085 Y

*(c) 7×7×⅜ A1085 Y*
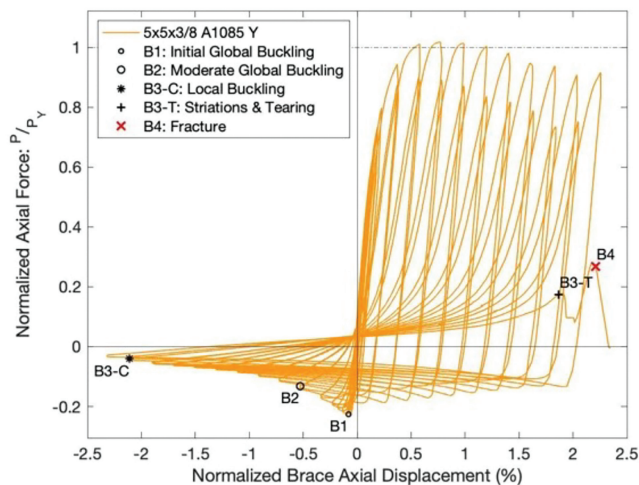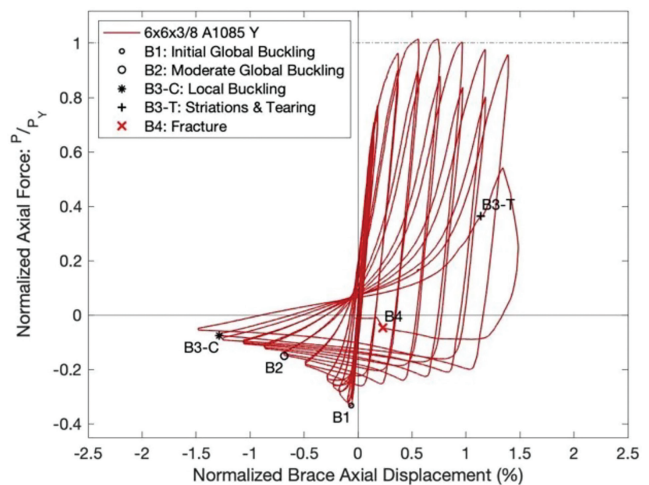
(d) 8×8×⅜ A1085 Y

Fig. 5. Axial force/deflection curve for four highlighted braces.

A maximum tensile force of 615.9 kips was reached at an axial displacement of 1.53 in. The brace eventually fractured during the tension portion of the first 3.25 in. target displacement cycle at an axial displacement of 2.31 in.

Specimen 8×8×⅜ A1085 Y buckled at a compressive force of 328.8 kips, which was the maximum compressive force, and an axial displacement of 0.31 in. The maximum tensile force achieved was 672.6 kips at an axial displacement of 1.2 in. Local cupping was initially observed at an axial displacement of 1.68 in. As the brace was cycled into tension during the second 2.25 in. target-displacement cycle, striations and tearing developed at the center of the brace. The tearing spread across the east and bottom walls of the tube, leaving the west wall and much of the top wall intact. Complete fracture occurred at an axial displacement of about 2.18 in.

Figure 6 shows the damage state of cupping just prior to brace tearing and fracture as well as the deformation at which this state occurred. Together, Figures 5 and 6 show that the severe cupping state B3-C occurred at sequentially smaller compressive deformations as the b/t ratio increased. (Recall that the HSS sections with larger widths have increased b/t ratios because the thickness of the four specimens is the same.) Further, Figure 6 shows that cupping deformation are concentrated over a shorter length as the b/t ratio increased.

The length of cupping can be assessed relative to the specimen depth. The HSS5×5×⅜ and the HSS6×6×⅜ sections meet the high ductility demand slenderness limit, and the cupping is clearly distributed over a longer (approximate 6 in.) length. The HSS8×8×⅜ section has a higher b/t ratio, which exceeds both the highly and moderately

(a) 5×5×⅜ A1085 Y

(b) 6×6×⅜ A1085 Y

(c) 7×7×⅜ A1085 Y
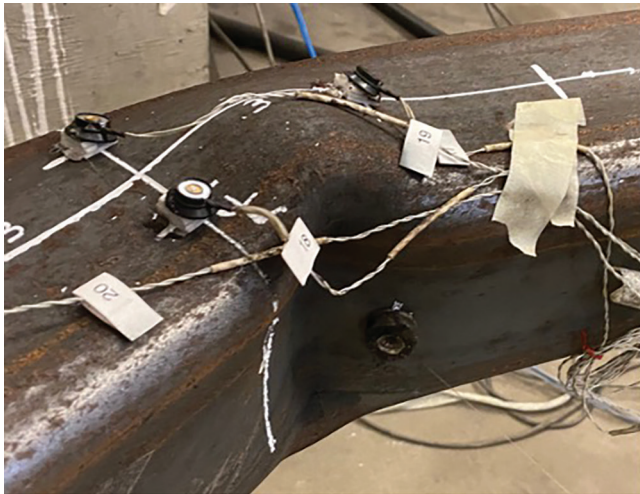
(d) 8×8×⅜ A1085 Y

Fig. 6. Severe cupping (state B3-C) just prior to tearing for the four highlighted specimens.

ductile slenderness limits; its cupping is distributed over a length that is approximately one-third of the highly ductile sections—that is, approximately 2 in. The largest inelastic strains develop in the cupped region, but the strain is distributed over a shorter length with larger b/t ratios, which leads to earlier fracture.

Impact of Loading History

The series III tests evaluated three different loading protocols; specifically, it compares chevron (compression-dominated) and near-fault (tension-dominated) test protocols with the conventional symmetric ATC-24 protocol used for the rest of the tests. Figure 7 shows the force-deflection behavior of A1085 5×5×⅜ Y braces tested under the compression-dominant, chevron, and tension-dominant, or near-fault, protocol. Figures 7(a) and 7(b) are compared to Figure 5(a) to evaluate the impact of the three different load histories on the response of the specimens. The chevron test shown in Figure 7(a) ran out of actuator stroke in compression well before specimen failure, and large tensile deformations were then applied to induce brace fracture. The near-fault protocol was completed to failure. The chevron and near-fault hysteretic behaviors are more one-sided than the ATC-24 protocol test. However, beyond this obvious difference, the behavior is very similar. Note the ATC-24 test achieved +2.25% axial deformation prior to brace fracture, and this resulted in 4.5% axial deformation range. The chevron test achieved −3.25% and 1.5% for a 4.75% range. The near fault achieved −1.5% and +3.25% for a 4.75% range. The maximum compressive forces were 98.4 kips, 93.3 kips, and 95.4 kips, respectively. The maximum tensile forces were 432.4 kips, 409.1 kips, and 464.2 kips.

There is very little difference in the post-yield (i.e.,

inelastic) behavior for the three displacement histories used in this study. The resistance of the specimens subjected to the near-fault protocol is slightly larger than the same specimen subjected to either of the other two histories. This difference is most likely due to the greater strain hardening with the near-fault protocol. The deformation range is similar in all cases but slightly smaller for the symmetric ATC-24 load history. This suggests that the symmetric ATC-24 test protocol is the more damaging than the other two for a given drift range.

Similar tests were performed with HSS7×7×⅜ and HSS8×8×⅜ braces with the same general results. This quite clearly shows that focusing on the total deformation range rather than the maximum brace deformation is a rational way of evaluation brace deformation capacity. This has been noted in other prior studies (Lehman et al., 2008).

Series IV consisted of three tests of these same three brace sizes with shorter brace lengths to clearly evaluate the impact of Kl/r on brace response. Figure 8 shows the force-deformation behaviors of the three shorter brace lengths and these figures can be compared to longer brace lengths in Figures 5(a), 5(b), and 5(c).

These specimens were subjected to that ATC-24 deformation protocol, which was adapted to the shorter brace length by adjusting the yield displacement. The 5×5×⅜ A1085 Y Short test specimen developed a maximum compressive force of 140.8 kips and a maximum tensile force of 438.6 kips. This buckling force is larger than the 98.4 kips achieved with 5×5×⅜ A1085 Y because of the smaller KL/r value, but the tensile resistance was similar at 443.6 kips. The axial deformations varied from −2% to 1.6% for an axial deformation range of 3.6% compared to 4.5% achieved by the longer specimen.
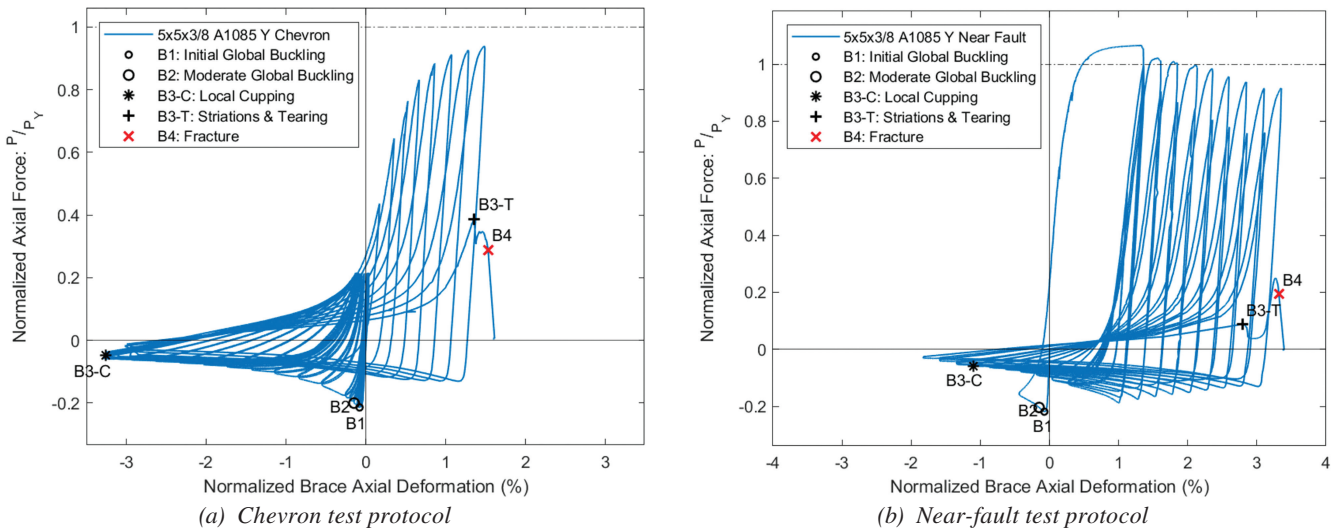

(a) Chevron test protocol

(b) Near-fault test protocol

Fig. 7. Near-fault and chevron test protocol with A1085 5×5×⅜ braces.

The 7×7×⅜ A1085 Y Short test specimen developed a compressive force of 327.9 kips and tensile force of 617.5 kips. The longer specimen, 7×7×⅜ A1085 Y, developed a 254.9 kip compressive force due to its larger KL/r value and a similar tensile force of 615.9 kips. The shorter specimen developed an axial deformation range of approximately 1.75%, while the longer specimen achieved approximately 2.75%.

Specimen 8×8×⅜ A1085 Y Short developed a compressive force of 393.6 kips and a maximum tensile force of 666.4 kips. The companion long specimen, 8×8×⅜ A1085 Y, developed a 328.8 kip compressive force due to its larger KL/r value and a similar tensile resistance of 672.6 kips.

The axial deformation range for the short and long specimen was similar at approximately 1.5%.

These comparisons clearly show that the normalized inelastic deformation capacity tends to be smaller for shorter specimens, and examination of the photos of the cupped regions suggests that the probable cause is the plastic hinging and cupping of the buckled braced that is concentrated over a shorter length with shorter braces. This result is logical. Cupping is caused by plastic hinging under compressive loading. The length of the cupped region occurs over a shorter length for shorter braces due to the local deformations in the shorter plastic-hinge region.
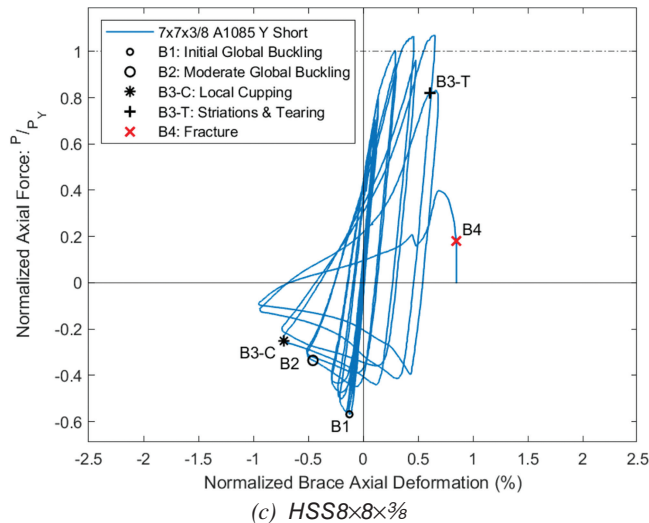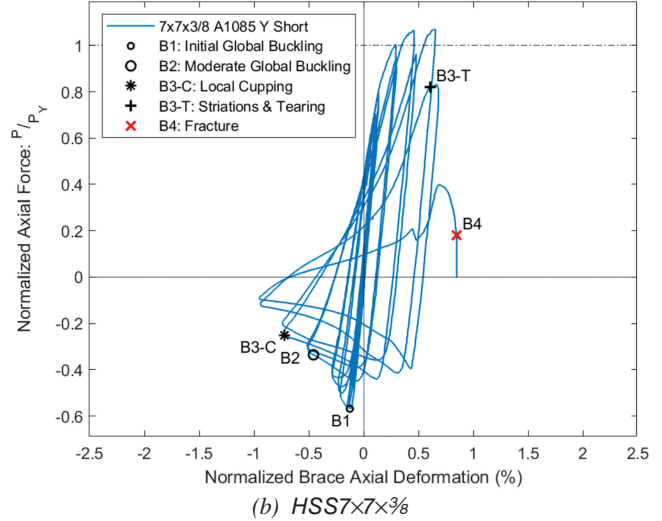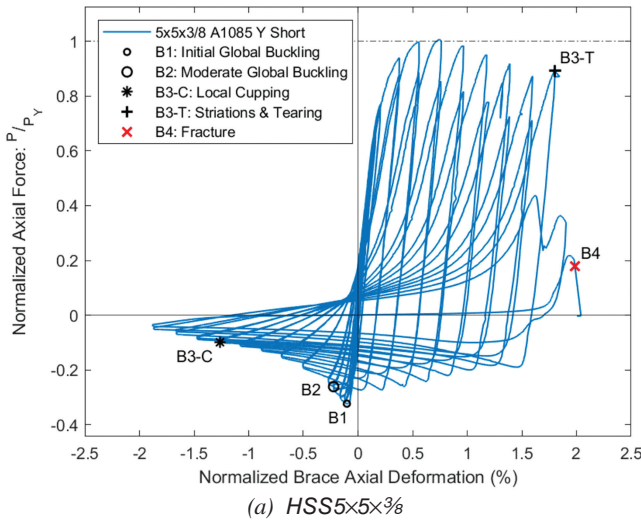

(a) HSS5×5×⅜

(b) HSS7×7×⅜

(c) HSS8×8×⅜

Fig. 8. Effect of shorter brace length.

EFFECT OF LOCAL SLENDERNESS OF BRACED FRAME DESIGN

Inelastic axial deformation of HSS braces is the primary yield mechanism in concentrically braced frames (CBFs). Through yielding in tension, buckling in compression, and post-buckling deformation, the brace is the main source of energy dissipation and inelastic deformation needed to resist demands from major earthquakes. As the brace experiences large axial deformations due to story drift, the midspan of the buckled brace forms a plastic hinge, and the brace develops local deformations or local cupping, which will ultimately lead to brace fracture. The ability to withstand large inelastic deformations without brace fracture is the basis of good seismic performance. The local compactness ratio, b/t, and global slenderness ratio, KL/r, have a significant impact on the initiation of local cupping and fracture of HSS braces. An HSS brace that has smaller local slenderness, b/t, and a larger global slenderness, KL/r, normally develops larger inelastic deformations prior to local cupping and fracture and that cupping is spread over a longer length.

Deformation demands for CBFs are usually stated in terms of story drift. As a result, the axial deformations for each test were converted to story drifts in Table 4, assuming that the total story drift is a result of the brace; this is a conservative approximation as additional deformation results from gusset plate yielding and frame action. As noted with prior discussion and shown in Figure 1, story drift and drift range are conservatively estimated as two times the normalized axial deformations.

For SCBFs, story-drift demand is estimated as +2.5% in AISC 341-22 (AISC, 2022). There is no specific limit postulated for OCBFs, but it is expected to be less than that for SCBFs since their response modification factor, R, is smaller and the resulting seismic design force is significantly larger. In addition, OCBFs are not permitted in high-seismic regions, and, as such, have received less attention in the literature, suggesting this system should be considered in future studies.

In a past study, Hsiao performed research that provides some insight on this expected demand (Hsiao et al., 2013). In that study, CBFs were designed to different resistance levels with R values between 3 and 8 for the seismic hazard in Seattle, Washington. The buildings were designed to seismic design standards for 3-, 8-, and 20-story height with the floor plans used for the SAC Steel Project (FEMA, 2000). In the study by Hsaio et al., SCBF requirements (geometric limits on the framing members as well as the brace, connection design) were used for all of the simulation models. Validated nonlinear models were developed to simulate the inelastic deformation of the brace, the frame and the connections including brace yielding, buckling, post-buckling, fracture, and post-fracture performance. The models were verified and calibrated to measured behavior from experimental research. Then 20 earthquake acceleration records were selected and scaled to the to the seismic hazard for the building location for a 2% probability of exceedance in 50 years and 10% probability of exceedance in 50 years seismic events. Nonlinear response history analyses were performed, and statistical evaluation of the response and expected damage were made. Figure 9 is a plot of the average maximum story drift for each level of the structure for the various building heights, design criteria, and seismic hazard. The plot clearly shows that the drift demand depends on the seismic event, the value of R, and the number of stories. Because the latter is not accounted for the building code, it will not be discussed here.

SCBFs currently have an R value of 6, and Figure 9 shows a 2.5% story-drift limit is about right for the three-story SCBFs. For taller buildings the average maximum story drift (MSD in Figure 9) is less than 1% for $R = 6$ and the 2% probability of exceedance in 50-year event.

OCBFs are designed for a response modification factor of 3.25 (simplified to 3 here), and Figure 9 would suggest that this requires a deformation capacity of about 1.0%
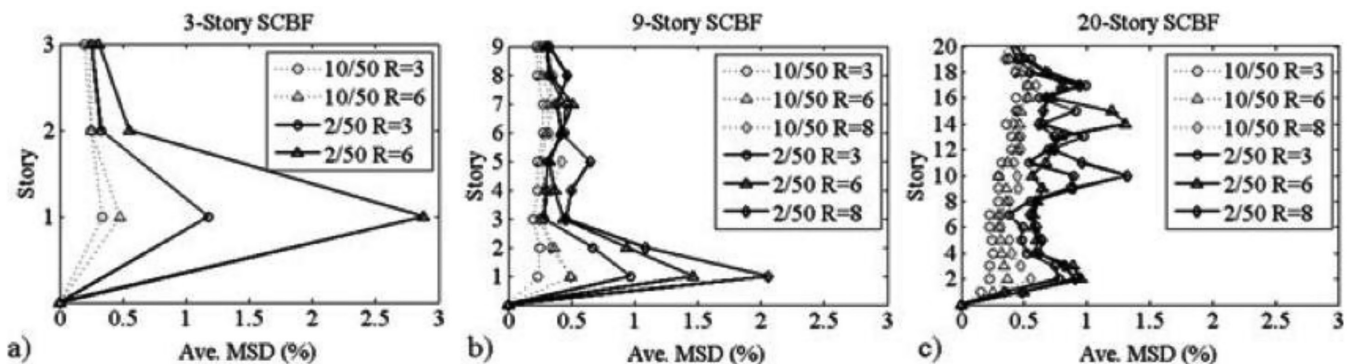

Fig. 9. Average maximum seismic response of OCBF and SCBFs (Hsiao et al., 2013b).

story drift prior to brace fracture for all three buildings. The experimental data discussed earlier show that story-drift range is a more accurate measure of the deformation capacity of an HSS brace because it is not influenced greatly by test protocol or seismic excitation. Thus, a 2.5% story-drift target in one direction for SCBFs is expressed as a story-drift range of 5%. The prior analysis does not provide data on drift range, but the maximum story drift of 2.5% implies a drift range less than 5%. These data are for a single location and should not be considered conclusive, but the data suggest that a maximum story-drift demand of approximately 2.5% is appropriate for SCBFs and a demand of 1.0% is appropriate for OCBFs.

Figure 10 shows the relationship between local compactness and story-drift range from the test data of this experimental research study. The measured yield stress is used to plot the data point for each specimen. The figure shows that a decrease in the local compactness ratio is associated with an increase in story-drift range. This figure clearly shows the importance of local slenderness limits for ensuring the inelastic deformation capacity of CBFs. All specimens meeting the highly ductile limit achieved a story-drift range of above 5%, indicating that the current highly ductile limit is sufficient and slightly conservative. Additionally, all the specimens achieved the 2.0% drift range as proposed for the moderately ductile limit and OCBF design with $1.0\sqrt{\dfrac{E}{R_yF_y}}$ as the local slenderness limit. Using this limit should provide satisfactory OCBF performance and greatly increase

the number of rectangular HSS braces that are suitable for OCBF design. The figure includes the long (238 in.) specimens as well as both A500C and A1085 tubes; shorter specimens would have somewhat reduced deformation capacity as noted earlier.

Figure 11 illustrates the effect of the KL/r ratio. All the A500C and A1085 specimens that meet the AISC 341 highly ductile local compactness requirement achieved a story-drift range of at least 5%, regardless of value of KL/r.

Figures 10 and 11 show that the deformability of HSS braces depends on the local slenderness ratio, b/t, and the global slenderness ratio, KL/r. The scatter in Figure 10 around a single value of b/t is largely due to differences in KL/r. Likewise, the scatter in Figure 11 is largely due to differences in b/t. The effects of these ratios are not independent of one another, and their interaction should be considered in design limits and numerical models simulating buckling brace behavior.

SUMMARY AND CONCLUSIONS

ASTM A500C and A1085 rectangular HSS sections are used for braces used in CBFs. In comparison with the A500C standard, HSS sections meeting the A1085 standard must satisfy a tighter tolerance on wall thickness and maximum yield stress, as well as meet a minimum CVN toughness. In comparison to A500C HSS sections, A1085 HSS sections are newer (introduced in 2013) and therefore are not as common in structural steel construction. The
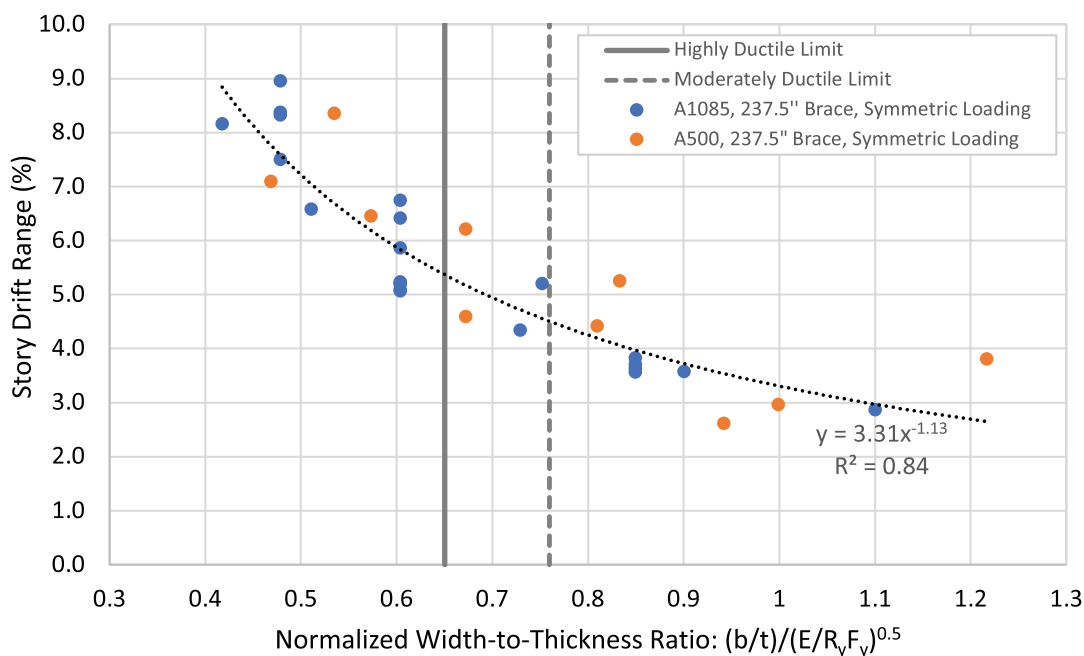

Fig. 10. Story-drift range vs. normalized width-to-thickness ratio.

tolerances on the A1085 HSS braces make them particularly attractive for seismic design because of the control on the geometry, toughness, and strength, yet there have been few tests of CBFs using A1085 HSS braces. As such, this research study was undertaken to investigate the differences in the two steel grades and the effect of those differences on the cyclic axial inelastic behavior of the brace and, therefore, the CBF.

Large-scale experiments and material testing were completed at the University of Washington Structural Engineering Testing Laboratory. Forty-one specimens were tested. The specimens were tested in four series. The first two series evaluated both A500 and A1085 HSS braces with b/t ratios ranging from of 9 to 25.7 and KL/r ratios ranging from about 60 to 127. The range of b/t values also permitted a study of the current limits in AISC 341 (2022) for high and moderate ductility limits, with the high ductility limit being set for SCBFs and the moderate ductility limit for OCBFs. In addition, series 3 and 4 tests permitted a direct comparison of several other study parameters, including (1) type of HSS (A500C or A1085); (2) HSS producer; (3) global slenderness ratio, KL/r; (4) local slenderness ratio, b/t; and (5) loading protocol (symmetric or chevron or near fault). The cyclic response of each brace specimens was analyzed to assess deformation capacity, energy dissipation capacity, and variations between manufacturers and materials.

The major conclusions from this work include:

- Deformability: The ductility (and energy dissipation capacity) of HSS bracing members is most significantly affected by both the local and global slenderness ratios (b/t and KL/r), which are interdependent.

- Cyclic response: The cyclic deformation capacity and energy dissipation increases with a decrease in local slenderness ratios and increase in global slenderness ratio.

- Steel grade: The variability between producers of A500C and A1085 were negligible. The variation in wall thickness was slightly greater for A500C braces, and A1085 have somewhat greater CVN toughness, but material properties were not significantly different.

- Local and global slenderness ratios: These ratios affect system deformability. Identical braces with identical b/t ratios provide greater inelastic deformation capacity with larger KL/r. Braces with similar KL/r will have more deformation capacity as the b/t ratios decreases.

- Deformation range: The defortmation range is a key engineering demand parameter for buckling braces. Under symmetric, cyclic loading, the response of the brace depends on the tension capacity, and the fracture life of the brace is determined by the response in compression, as affected by local and global slenderness limits. The maximum tensile deformation depends on
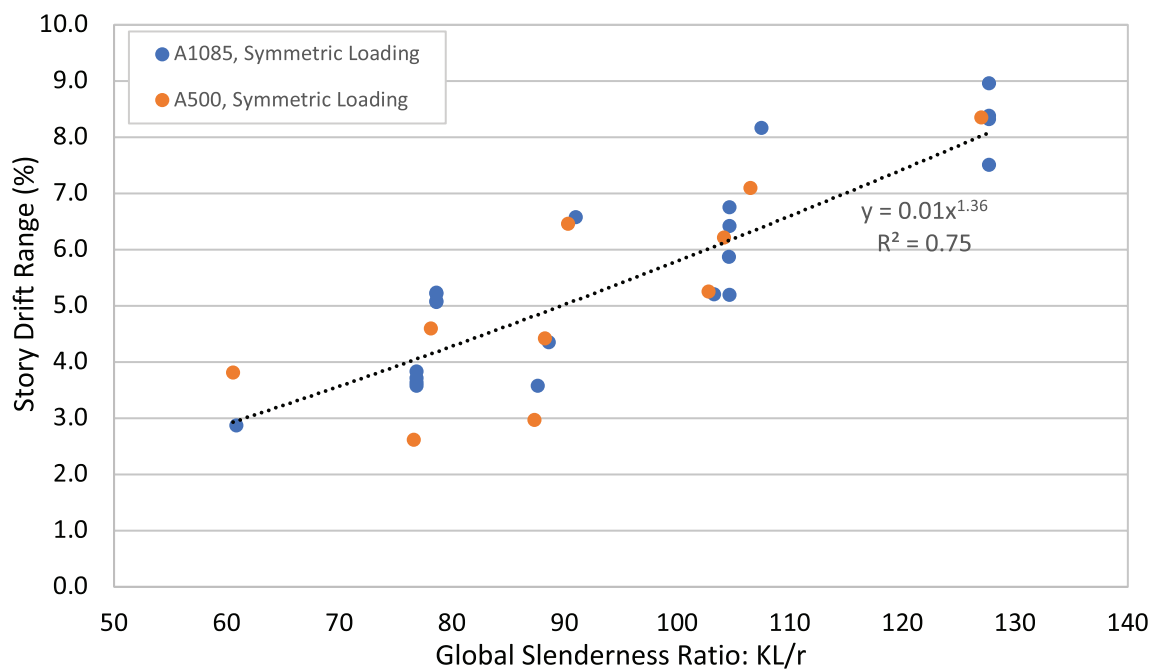

Fig. 11. Story drift range vs. global slenderness.

imposed deformation history, and therefore, the highest tensile displacements were measured for the symmetric and pulse-type (tension-dominated) history. However, the deformation range does not depend on imposed displacement history. Therefore, story drift range is a better measure of the maximum deformation capacity, rather than the maximum drift in any single direction. Further, the symmetric protocol provides a more conservative estimate of deformation capacity than the other protocols.

Additional research is needed to fully explore the range of b/t ratios for both types of HSS braces. In particular, HSS braces with larger b/t ratios (above 25) should be tested to investigate the possibility of increasing the moderately ductile limit from $0.76\sqrt{\dfrac{E}{R_yF_y}}$ to $1.0\dfrac{E}{R_yF_y}$; the latter term is supported by the results presented herein. In addition, the results of these tests should be used to update nonlinear models to investigate the impact of changes in the b/t limits on building performance. In addition, the research clearly shows that both local slenderness and global slenderness impact the deformability of square HSS braces. This interaction might be included in future revisions of AISC 341, Table D1.1a. Finally, the results of any future research study should be combined with this data to revisit both the highly ductile and the moderately ductile limits in AISC 341.

ACKNOWLEDGMENTS

REFERENCES

AISC (2022), *Seismic Provisions for Structural Steel Buildings*, ANSI/AISC 341-22, American Institute of Steel Construction, Chicago, Ill.

ASTM (2019), *Standard Specification for High-Strength Structural Bolts and Assemblies, Steel and Alloy Steel, Heat Treated, Inch Dimensions 120 ksi and 150 ksi Minimum Tensile Strength, and Metric Dimensions 830 MPa and 1040 MPa Minimum Tensile Strength*, ASTM F3125/F3125M-19, ASTM International, West Conshohocken, Pa.

ASTM (2020), *Standard Specification for Structural Steel Shapes*, ASTM A992/A992M-20, ASTM International, West Conshohocken, Pa.

ASTM (2021), *Standard Specification for Cold-Formed Welded and Seamless Carbon Steel Structural Tubing in Rounds and Shapes*, ASTM A500/500M-21a, ASTM International, West Conshohocken, Pa.

ASTM (2022), *Standard Specification for Cold-Formed Welded Carbon Steel Hollow Structural Sections (HSS)*, ASTM A1085/1085M-22, ASTM International, West Conshohocken, Pa.

ASTM (2023), *Standard Test Methods and Definitions for Mechanical Testing of Steel Products*, ASTM A370-23, ASTM International, West Conshohocken, Pa.

ATC (1992), "Guidelines for Cyclic Seismic Testing of Components of Steel Structures for Buildings," Report ATC-24, Applied Technology Council, Redwood City, Calif.

Ballard, R. (2015), "Impact of Connection Type on Performance of Non-Seismic Concentrically Braced Frames," MS Thesis, University of Washington, Seattle, Wash.

Clark, K.A. (2009), "Experimental Performance of Multi-Story X-Braced SCBF Systems," MS Thesis, University of Washington, Seattle, Wash.

Fell, B.V., Kanvinde, A.M., Deierlein, G.G., and Myers, A.T. (2009), "Experimental Investigation of Inelastic Cyclic Buckling and Fracture of Steel Braces," *Journal of Structural Engineering*, Vol. 135, No. 1, pp. 19–32.

FEMA (2000), "State of the Art Report on Systems Performance of Steel Moment Frames Subject to Earthquake Ground Shaking," FEMA 355C, Federal Emergency Management Agency, Washington, D.C.

Han, S.-W., Kim, W. T., and Foutch, D.A. (2007), "Seismic Behavior of HSS Bracing Members According to Width-Thickness Ratio under Symmetric Cyclic Loading," *Journal of Structural Engineering*, Vol. 133, No. 2, pp. 264–273.

Herman, D.J. (2007), "Further Improvements on an Understanding of Special Concentrically Braced Frame Systems," MS Thesis, University of Washington, Seattle, Wash.

Hsiao, P-C, Lehman, D.E., and Roeder, C.W. (2013), "Evaluation of Response Modification Coefficient and Collapse Potential of SCBFs," *Earthquake Engineering and Structural Dynamics,* Vol. 42, No. 10, pp. 1547–1564.

Ibarra, S.M. (2018), "Experimental Investigation of Chevron Special Concentrically Braced Frames with a Yielding Beam Plastic Mechanism," MS Thesis, University of Washington, Seattle, Wash.

Johnson, M. (2014), "Seismic Behavior of Bolted Connections in Non-Seismic Braced Frames," MS Thesis, University of Washington, Seattle, Wash.

Johnson, S.M. (2005), "Improved Seismic Performance of Special Concentrically Braced Frames," MS Thesis, University of Washington, Seattle, Wash.

Kotulka, B.A. (2007), "Analysis for a Design Guide on Gusset Plates Used in Special Concentrically Braced Frames," MS Thesis, University of Washington, Seattle, Wash.

Lee, S. (1988), "Seismic Behavior of Hollow and Concrete-Filled Square Tubular Bracing Members," Report UMCE 87-11, University of Michigan, Ann Arbor, Mich.

Lehman, D.E., Roeder, C.W., Herman, D., Johnson, S., and Kotulka, B., (2008), "Improved Seismic Performance of Gusset Plate Connections," *Journal of Structural Engineering*, ASCE, Vol. 134, No. 6, pp. 890–901.

Liu, Z. and Goel, S.C. (1987), "Investigation of Concrete-Filled Steel Tubes under Cyclic Bending and Buckling," University of Michigan, Ann Arbor, Mich.

Lumpkin, E.J. (2009), "Enhanced Seismic Performance of Multi-Story Special Concentrically Brace Frames Using a Balanced Design Procedure," MS Thesis, University of Washington, Seattle, Wash.

MTS (2011), MTS Model 793.10 MuliPurpose TestWare and Series 793 Application Software, MTS Systems Corporation, Eden Prairie, Minn.

Powell, J.A. (2010), "Evaluation of Special Concentrically Braced Frames for Improved Seismic Performance and Constructability," MS Thesis, University of Washington, Seattle, Wash.

Richard, J. (2009), "Etude du Comportemenet Sismique de Bâtiments Industriels aveć Systèmes de Contreventement en Acier de Faible Ductilitè," PhD Dissertation, Ecole Poly-technique de Montrèal, Montreal, Quebec, Canada.

Roeder, C., Sen, A., Terpstra, C., Ibarra, S. Liu, R., Lehman, D., and Berman, J. (2019), "Effect of Beam Yielding on Chevron Braced Frames," *Journal of Constructional Steel Research*, Vol. 159, pp. 428–441. DOI: 10.1016/j.jcsr.2019.04.04

Roeder, C.W., Lumpkin, E., and Lehman, D.E. (2011), "A Balanced Design Procedure for Special Concentrically Braced Frames," *Journal of Constructional Steel Research*, Vol. 62, pp. 1760–1776.

Roeder, C.W., Lumpkin, E., and Lehman, D.E. (2012), "Seismic Performance Assessment of Concentrically Braced Steel Frames," *Earthquake Spectra*, Vol. 28, No. 2, pp. 709–727.

Sen, A.D. (2014), "Seismic Performance of Chevron Concentrically Braced Frames with Weak Beams." MS Thesis, University of Washington, Seattle, Wash.

Sen, A.D. (2018), "New Methods for Seismic Performance Evaluation and Retrofit of Nonductile Concentrically Braced Frames," A dissertation submitted in partial fulfillment of degree of Doctor of Philosophy, University of Washington, Seattle, Wash.

Shaback, B. and Brown, T. (2003), "Behaviour of Square Hollow Structural Steel Braces with End Connections under Reversed Cyclic Axial Loading," *Canadian Journal of Civil Engineering*, Vol. 30, No. 4, pp. 745–753.

Swatosh, M.A. (2016), "Seismic Evaluation and Retrofit of Concentrically Braced Frames," MS Thesis, University of Washington, Seattle, Wash.

Sloat, D.A. (2014), "Evaluation and Retrofit of Non-Capacity Designed Braced Frames," MS Thesis, University of Washington, Seattle, Wash.

Yang, F. and Mahin, S.A. (2005), *Limiting Net Section Failure in Slotted HSS Braces*, Structural Steel Education Council, Moraga, Calif.

Uriz, P. and Mahin, S.A. (2008), "Toward Earthquake-Resistant Design of Concentrically Braced Steel-Frame Structures," PEER 2008/08, Pacific Earthquake Engineering Research Center, Berkeley, Calif.